Contents

Part I

ActiveAx

Chapter 1

Scan/rescan reproducibility in the corpus callosum and spinal cord

1.1 Introduction

In the previous chapter we have presented an initial attempt of implementing our $\mathcal{SF}$ ActiveAx on a clinical system. that can be acquired in under 25 minutes scan time. We found that our 25 minute long $\mathcal{SF}$ protocol can produce comparable results to the 3 times longer $\mathcal{OI}$ method. Our initial work was focussed only on the optimisation of the acquisition protocol. However, it is clear that several diffusion protocol independent imaging factors, such as accurate positioning or spatial resolution, contribute significantly to the goodness of our parameter estimates. In this chapter we address several of those additional imaging parameters. Our main aim is to improve SNR and spatial resolution of our dataset in order to maximise accuracy and reproducibility of our microstructure maps.

In detail, the changes compared to the protocol in Chapter **??** are as follows:

Imaging: We use of a small field-of-view (FOV) imaging sequence to increase both image resolution and SNR.

Positioning: We develop a new method to better align the image volume with the dominant fibre direction of the CC using fast DTI tractography directly on the scanner console.

Acquisition: We extend the signal model used in the optimisation and fitting to allow the use of shortest available echo time (TE) for different combination of diffusion gradient pulse duration (δ) and diffusion time (Δ). Furthermore we increase the nominal maximal gradient strength to 87mT/m using the the modified scanner software we developed for the QSI study in Chapter **??**. The combined effect lower TE and stronger gradient will increase SNR and aid the performance of the parameter fitting routine.

We analyse our new imaging pipeline in 5 healthy volunteers, who were scanned

at two different timepoint to assess both intra- and inter-subject reproducibility. Furthermore we test our protocol in the cervical spine of one healthy volunteer.

1.2   Methods & Experiments

Protocol optimisation

We use the same $a\mathcal{SF}$ optimisation as described in Section **??** of Chapter **??**, but with one single modification: we adapt the tissue model to include an additional T2 decay factor that accounts for signal loss in the DWI with respect to the TE. For simplicity, we assume here a mono-exponential T2 decay of the signal. Previously, the TE was governed by the maximum TE in the whole protocol. This modification now allows the dynamic use of TEs for different (δ, Δ) settings in the protocol optimisation. This has the advantage of effectively reducing the TE in the low DWI acquisition, which improves greatly improves the SNR in those acquisitions.

We carry out the optimisation using as before, assuming T2=70ms, which is typical for white matter (WM) in the CC **?**. We also use the scanner software modification we described in Chapter **??**, which allows to combine several orthogonal 62mT/m-gradients to increase the maximum gradient strength to 87mT/m. To improve directional resolution required for the fit of the diffusion direction, we add a single shell DTI acquisition (max b=800s/mm2, 1 b=0, 16 uniformly distributed directions) to the optimised protocol. The full set of parameters is given in Table **??**.

Data acquisition

We recruited 5 healthy volunteers (3 female, 2 male, mean age=28 +/-) to be scanned on a Philips Achieva 3TX scanner. All subjects were recalled for a second scan on a different day to assess the intra-subject reproducibility of the experiment. In each scan session we acquire a the optimised $\mathcal{SF}$ DWI protocol with following scan parameters: voxel size: 1x1x4mm3, FOV=96x96mm2, TR=6000ms, 2 averages, using an outer-volume suppressed ZOOM acquisition (**?**) to avoid fold-over artifacts.

The previous experiments have shown that our $\mathcal{SF}$ methods benefit from accurate alignment of the gradient scheme with respect to the dominant fibre direction. While standard T2w localizers are adequate to align the scan volume to anatomical reference, it offers no information about the WM fibre orientation. To aid slice positioning, we acquire a fast DTI scan in addition to the conventional scout scans. The scout-DTI imaging parameters are as follows: XXXXXXXXXXXXXx. We use the PRIDE tools directly on the scan console to place a ROI in the mid-sagittal slice of the CC and perform FACT tractography on the DTI dataset (FA threshold=0.45, angle threshold=YY). The tracts are then overlayed on the colour-coded FA map, rasterised, and resliced to obtain a new 1x1x1 image volume. We use the axial and coronal views of the tractography results to adjust the angulation of the $\mathcal{SF}$ image volume with respect to the observed tracts. Figure 1.1 shows an example of the final slice alignment based on both the structural localizer scan and tractography results.
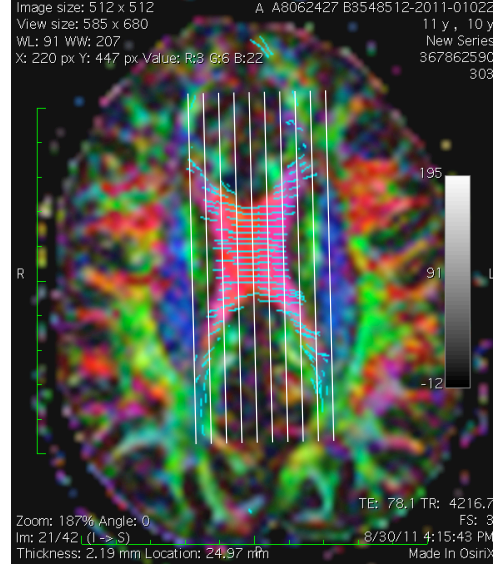
Since the whole scout-DTI processing is performed on the scanner console, the additional scan setup time by acquiring analysing the scout-DTI scan is kept to a minimum.
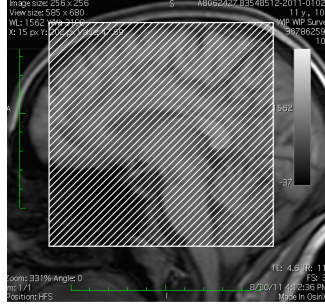
(a) Sagittal localizer
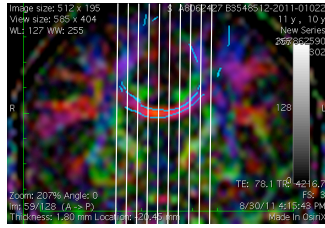
(b) Coronal FA map overlayed with tractography results (cyan lines)

(c) Axial FA map with overlayed tractography results (cyan lines)

Figure 1.1: Positioning of small FOV scans in white, overlayed on a sagittal scout image (a) and axial and coronal DTI tractography results (b&c).

Post-processing

We compensate for motion during the acquisition by aligning all scan volumes to the first b=0 image using the block-wise rigid registration algorithm (**?**) implemented in (**?**). However, since the diffusion weighted images provide little contrast in non-coherently aligned WM tissue, we only register the interleaved b=0 images and apply the estimated transformation matrix to the subsequent intermediate b>0 images.

To ensure anatomical correspondence between scan and rescan, we then register the rescan dataset to the scan dataset (using rigid registration) using the transformation estimates from registering the first b=0 images of the two datasets. The transformation matrices for intra-scan motion and scan/rescan alignment are combined before applying them to the dataset to avoid unnecessary multiple interpolations. The data is then smoothed using the Unbiased Non-Local Means filter (**?**) with a filter radius of $3x3x1$.

Data analysis

We use the same fitting procedure as outlined in the previous chapters. However since we allowed for variable TE in each acquisition, we need to account for the

resulting differences in T2 single decay within the data. We therefore estimate the voxel-wise mono-exponential decay curve using a linear regression model based on the non-diffusion-weighted acquisitions. The predicted MR signal S from the tissue model is then adjusted based on its TEs by:

$$S' = S * exp(TE/T2). \qquad (1.1)$$

The adjusted signal S' is then used to compute the rician log-likelihood with the observed signal as previously. We computed the posterior distributions of the model parameters using an MCMC method on a voxel-by-voxel basis. From the mean of the posterior distribution we compute the the axon diameter index a and axonal density index ρ=f/π/a^2. In addition we also fitted the diffusion tensor to the 16-direction DTI data and derive the principal eigenvectors $v1$–$v3$ and scalar maps of FA, MD, AD, RD. The fitting routine is implemented using the open-source Camino toolkit (Cook et al., 2006).

ROI analysis

In each subject we manually segmented roughly the CC on the mid-sagittal slice. We then remove all voxels from the CC mask with FA<0.5 appear to exclude voxels with more than one single fibre orientation or significant CSF contamination from the analysis. We further exclude voxel where v1 deviated more than 10 degrees from the left-right fibre orientation we assumed in the protocol optimisation. The CC segmentation is then divided in 10 equidistant regions along the anterior-posterior baseline similar to **?**. Figure **??** shows an example of the CC subdivision in one subject. Mean a and ρ indices are then computed for each CC subdivision in each of the 10 datasets. Scan/rescan agreement is assessed visually as well as it is quantified by computing the intraclass correlation coefficient (ICC) (**?**) over the whole CC and in each region of interest (ROI). To investigate the correlation between DTI metrics and a and ρ, we pool all values in the CC ROI of all subjects separately for scan and rescan and report the robust correlation coefficient (**?**). All statistical processing was performed using the software R(**?**) with packages 'ICC'(**?**) and 'robust'(**?**).

1.3   Results

Axon diameter and axon density indices in the CC

Figure 1.7 shows side-by-side scan/rescan maps of a and ρ for all five subjects. Figure 1.4 summarizes the mean a and ρ parameters measured in each ROI for all five subjects. In all subjects we can clearly see the variation along AP we expect from previous experiment and earlier studies (Alexander et al., 2010). Furthermore, in comparison with those earlier results, our maps appear considerably less noisy and show improved contrast between different CC regions. Consistent with our previous results, we estimate values of a in the range of 5–15μm. The largest a estimates are found in the midbody of the CC. The smallest a values are found in the splenium <8μm and the anterior part of the genu (9–11μm). The axon density index ρ is reciprocal to the a trends, with ρ being largest in the anterior genu and posterior splenium regions (XX–XY) and smallest in the body and isthmus of the CC. Axons too large!! The a and

ρ pattern we observe here agrees very well with the microstructure that is seen in excised human CC tissue samples.

Unlike in the previous experiments, the high spatial resolution here provides a large number of voxels that are completely contained in the CC. As a consequence, the CC can be easily distinguished from surrounding tissue and the tissue parameter estimates are less influenced by CSF contamination, particularly in the thinning part of the CC (B3–S1). This is beneficial for subjects with smaller CC such as found in s2 & s3, but becomes even more important in view of future applications in patients with neurological diseases such as MS or Alzheimers disease, who often suffer from severe CC atrophy.
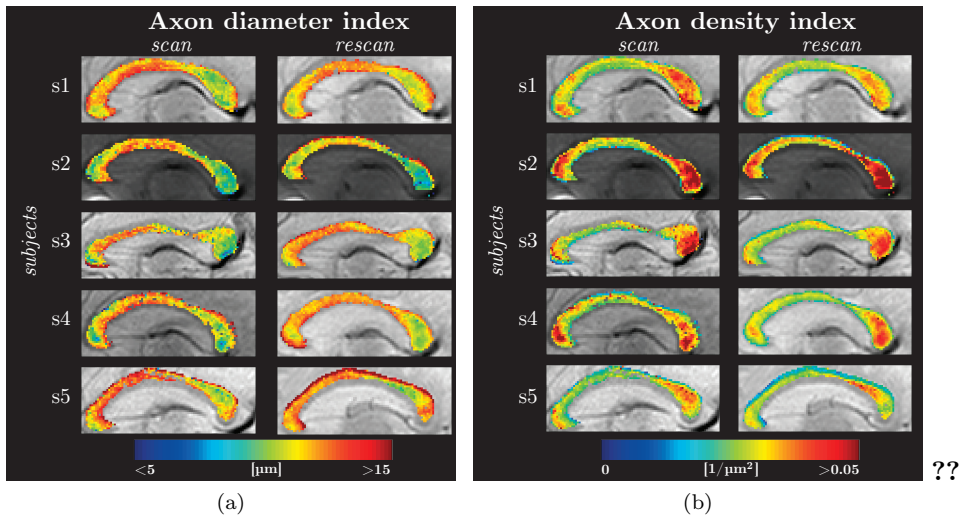

(a)   (b)

Figure 1.2: XX (continued)

Inter- & Intra-subject reproducibility

A simple visual comparision of scan and rescan maps suggest that ROI-wise microstructure estimates are very consistent between the five subjects. As shown in Figure **??**, the average results over all 5 subjects are very similar between scan and rescan experiment, both in the average trend as well as in the observed standard deviation. Moreover, both a and ρ show very little variation from the mean over all subjects. Inter-subject variation is lower in the mid-body and the proximal genu regions (G2–G3) than in the more distal anterior and posterior regions. The Bland-Altman plots shown in Figure **??** show good scan/rescan variation independent of parameter estimate with the majority of ROI estimates within the 95% confidence interval. Few ROI outliers which exhibit rather scan/rescan large variation. Scan/rescan variation appears unsystematic in a. However in ρ, the large axon density estimates appear more unstable than smaller ρ values. Outliers appear mostly in the most distal G1 and S3 regions. Such large variations might indicate cardiac pulsation artifacts as these regions are closest to the adjacent Arteria Cerebralis.

Table **??** presents the ICC values ICC for whole CC and individual ROIs.

For both a and ρ, we find the scan/rescan agreement being 'moderate' or better for both whole CC values and most ROIs. As noted before, the lowest ICC values are found in boundary regions (G1) or in the thin proximal part of the CC, which are most affected by imaging and analysis artefacts. Both Bland-Altman analysis as well as the ICC suggests that estimated values in those ROIs appear more prone to error and must be interpreted with caution.
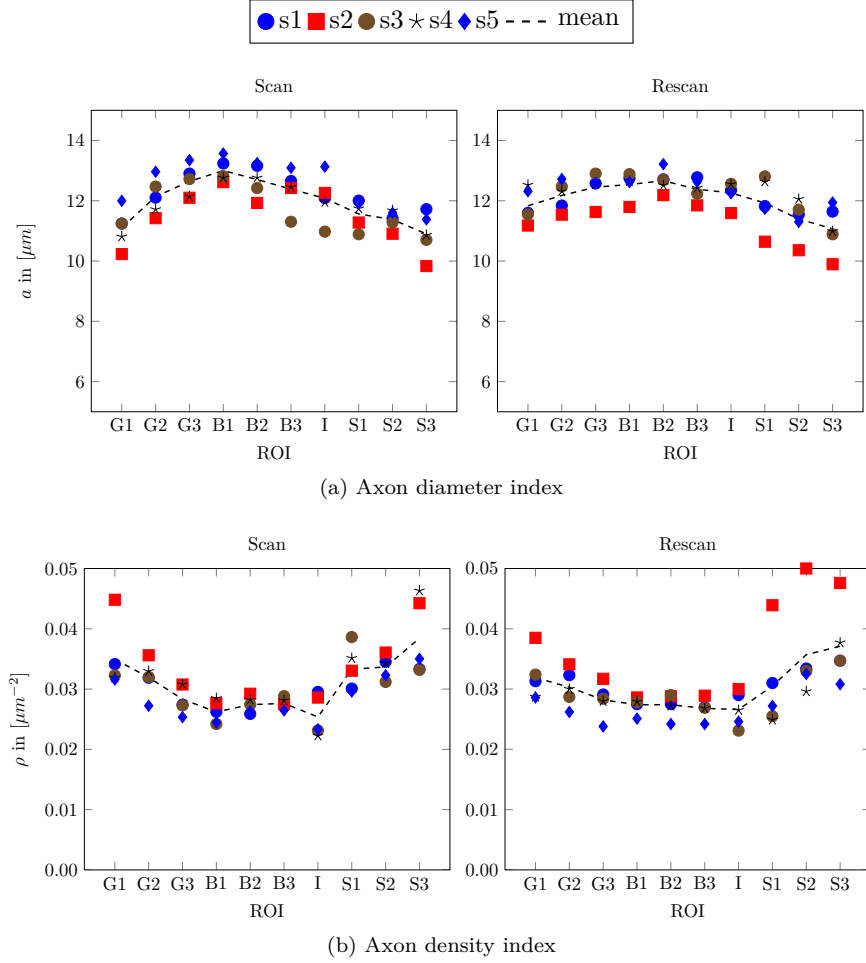

(a) Axon diameter index

(b) Axon density index

Figure 1.3: Scatter plots of axon diameter (a) and axon density (ρ) indices in all 5 subjects in individual ROIs. The dashed line shows the average over all subjects.

Correlation with DTI metrics

Figure 1.6 presents the correlation between the standard DTI metrics and the a and ρ estimates. The correlations we see here agree with the findings of (Barazany et al., 2009) and (Alexander et al., 2010). While MD is not correlated either of the microstructure indices, the directional diffusivities AD and RD both show moderate correlations with a and ρ. Of course it is not sur-

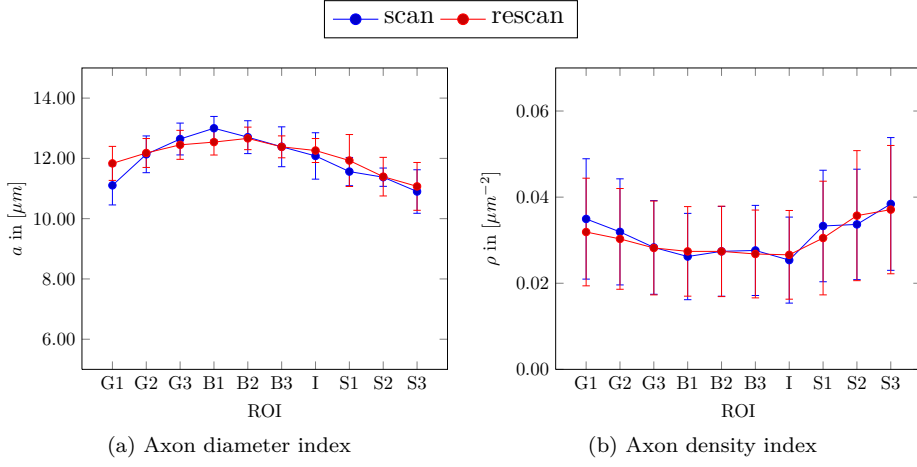(a) Axon diameter index　　　　(b) Axon density index

Figure 1.4: Scatter plots of axon diameter (a) and axon density (ρ) indices in all 5 subjects in individual ROIs. The dashed line shows the average over all subjects.

Table 1.1: ICC values for whole CC and individual ROIs for a and ρ estimates.

	whole CC	G1	G2	G3	B1	B2	B3	I	S1	S2	S3
						Individual ROIs					
a	0.66 ■	0.14 ■	0.83 ■	0.56 ■	0.14 ■	0.81 ■	0.46 ■	-0.25 ■	-0.07 ■	0.70 ■	0.94 ■
ρ	0.79 ■	0.74 ■	0.77 ■	0.78 ■	0.44 ■	0.59 ■	0.34 ■	0.79 ■	-0.14 ■	0.34 ■	0.73 ■

Guidelines for agreement (**?**): ■ < 0.2: poor, ■ 0.2–0.4: fair, ■ 0.4–0.6: moderate, ■ 0.6–0.8: substantial, ■ > 0.8: almost perfect

prising to find *RD* negatively correlated with a and positively correlated with ρ respectively, as it is know both axonal packing density, and axon diameter all influence *RD* measurements (**?**). The observed correlation between *AD* and a (positive) and ρ (negative) is less intuitively explainable, however consistent with previous findings (Barazany et al., 2009; Alexander et al., 2010). Alexander et al. speculate that the increase of axon size and decrease of packing density are associated with lower fibre coherency, and thus are causing an increasing amount of diffusion impedance along the dominant diffusion direction. The correlation between AD and the a and ρ indices might also be the result of varying CSF contamination, since the regions high axon diameter are mostly found in the thinner midbody region are more affected by partial volume effects than those in genu and splenium. Since we find both *AD* and *RD* correlated with the a and ρ indices, their correlation with *FA* follows by definition.
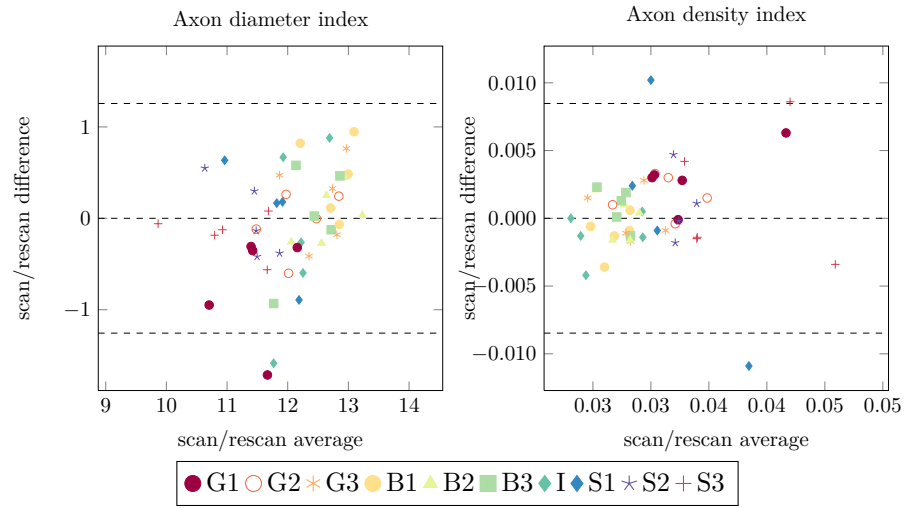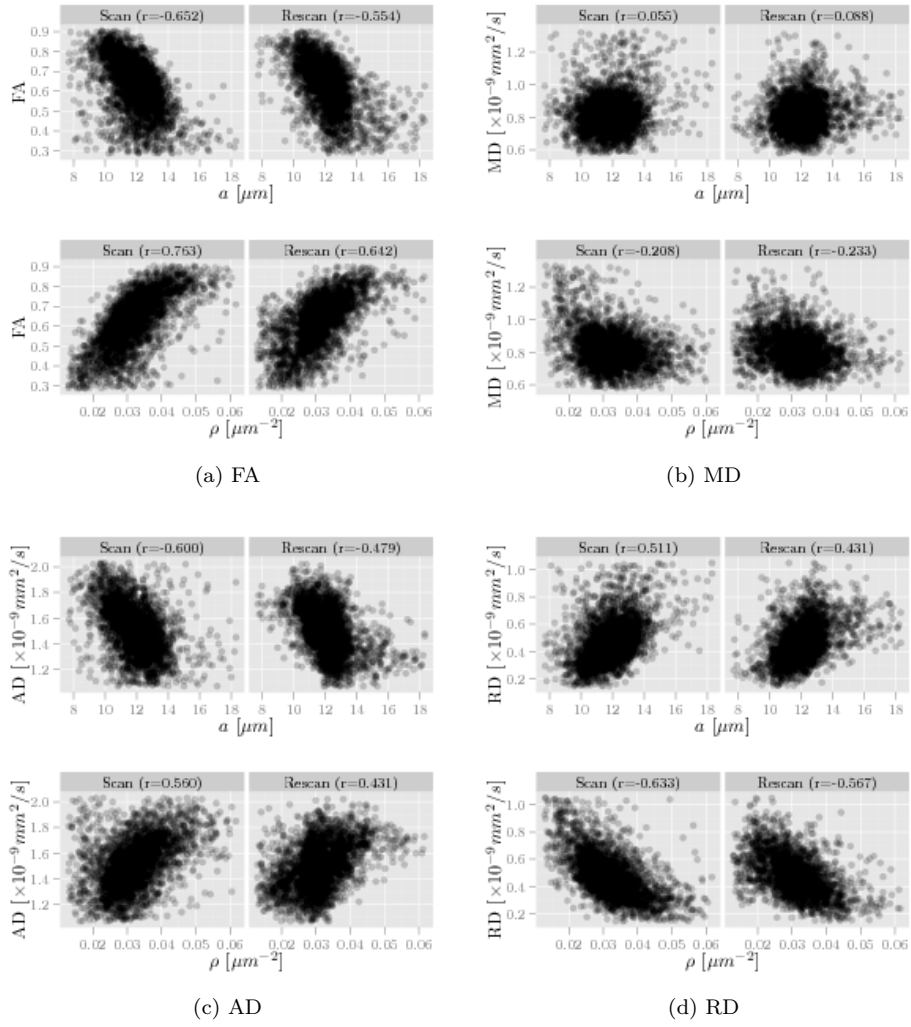
Figure 1.5: XX

(a) FA

(b) MD

(c) AD

(d) RD

Figure 1.6: XX

Axon diameter and axon density indices in the SC

Figure **??** shows the a and ρ maps acquired in one healthy volunteer. We clearly see the bilateral symmetry of the parameter maps as expected from the basic anatomy of the spinal cord. The estimates of a and ρ indices are within a similar range of values measured in the CC. Furthermore, both a and ρ allow good discrimination between motor and sensory WM tracts. The largest a (10.7 +/- $2\mu m$) and lowest ρ ($0.035 +/- 0.017 \mu m^{-2}$) are found in the lateral tract. The dorsal sensory tract shows the lowest a ($9.1 +- 1.3\mu m$) and highest ρ ($0.046 +/- 0.017\mu m^{-2}$). The contrast between LT and DC is consistent over several slices in our dataset and agrees with our earlier findings in fixed monkey cervical cord. Figure **??** also illustrates well the challenges in SC imaging. The posterior halo of low a is the result of motion artifacts during the acquisition which can be cause e.g. by swallowing or breathing. Cardiac motion also makes cardiac gating a neccesity, which in turn reduces the data we can acquire within the 25 minute windows and consequently reduced the SNR in our data. However, the results here show first evidence that our $a\mathcal{SF}$ protocol can be used succesfully in the SC application, despite the more challenging imaging environment.
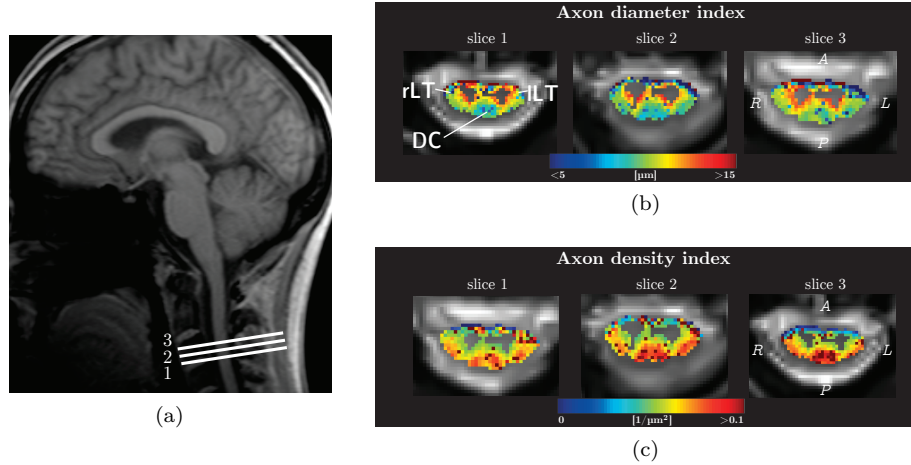

Figure 1.7: (a) SC slice alignment and (b&c) maps of a and ρ in one healthy volunteer. Annotations on the first result slice denote the location of the dorsal column (DC) and left and right lateral tracts (LT).

1.4   Discussion

This work presents a novel imaging and analysis pipeline for measuring axon diameter and density indices in the CC in-vivo, which expands on our $a\mathcal{SF}$ protocol optimisation we introduced in the previous chapter. We combined small FOV imaging and careful optimisation of the MR protocols and post-processing techniques to gain both high spatial resolution while maximising SNR. We show here axon diameter and axon density maps of better quality than previous studies have shown before. For the first time present results of a larger subject cohort of 5 subjects, allowing to infer scan and rescan reproducibilty with more

confidence. Our results show that a and ρ show very good reproducibility consistently over all investigated subjects. Furthermore, a first test of our protocol in healthy cervical produced compelling results that are in good agreement with our findings excised monkey cervical cord.

Limitations & further work

Interpretation of a and ρ The model we use here is a very simplistic approximation of the complex micro-anatomy of real biological tissue. The actual estimates of axon diameter and densities differ considerably from what is expected from histology or ex-vivo scans (Alexander et al., 2010). Most of this disparity can be explained by the limited gradient strength available on clinical system. With limited gradient strength, small axons cause very little signal attenuation and become indistinguishable from each other (**??**). Our simulation experiments in Chapter **??** show a limit of sensitivity of of 2–4μm even in the very idealised situation of perfectly aligned single-radius cylinders. Consequently, the a and ρ indices must not be seen as accurate reflections of the complete axon diameter distribution as they are likely driven only by a small number of large axons in the WM.

Other more complex models have been also been suggested, adding more tissue compartments, a distribution of axon diameters and/or permeable membranes. However, with the given limits both in scan time and gradient hardware, their practical value for in-vivo clinical applications is questionable. Recent studies e.g. by **?** have studied those complex models in the CC WM tissue with much more extensive dataset than we used here. Their findings suggest that the simple two compartment model explains diffusion in coherent WM tissue reasonably well. For our purpose of clinical adaptation, the model used here provides a good trade-off between explaining the diffusion in WM while keeping data requirements reasonably low. The shorter protocol we propose is an important step to enable more widespread adaptation of our imaging pipeline, which in turn will lead to a better understanding of its parameters interpretation.

Furthermore, alternative acquisition methods such as oscillating gradients (**??**), multiple wave-vector acquisitions (**??**) promise more sensitivity to smaller axon diameters. Recently **?** extended the protocol optimisation framework optimise the shape of the gradient waveforms to achieve a similar effect. The method we present here extends naturally to those other pulse sequences and can easily be combined with those frameworks to provide more discriminative axon diameter indices.

T2 estimation: We chose here to estimate T2 directly from the b=0 weighted images. Using this approach, we are limited to estimate rather high TEs due to the nature of the single shot EPI technique used here. Furthermore, due to the sparsity of the TEs samples, we can only account for mono-exponential T2-decay. A more comprehensive T2 decay curve could potentially be estimated using other imaging technquies (TFE, TSE). However, this would add significant scan time to our protocol. Furthermore, those techniques are not always anatomically aligned with the EPI diffusion scans, due to EPI induced distortions and require further registration, which might confound the results. A better T2 estimation could also be used to correct for T2 differences between intra- and extra-axonal compartments. Fitting a single T2 time to all compartments

could lead to errors in the f_{intra} estimates and might have an affect on our ρ parameter maps. While the tissue model extends easily to incorporate different T2s for different compartments.

Directional variation: In simulations we have seen that the $\mathcal{SF}$ protocols are severely affected by misalignment of the gradients with the dominant diffusion direction. To minimise this effect we use fast tractography to align the scan volume with the fibre direction in the CC. By design, the $\mathcal{SF}$ protocols have unsufficient directional resolution to estimate the diffusion direction correctly. We used here an additional DTI datatset to stabilise the fit of the diffusion directions. However, the directional resolution of the DTI dataset might not be ideal compared to the HARDI protocol such as $\mathcal{OI}$. While we the fit of the direction appears reasonable, mis-fit of the direction might artificially increase the estimates of axon diameter index.

Validation: We have validate our result here by comparision with previous reports of tissue parameter estimates by diffusion MRI and independent histopathology. While several systematic reports of the tissue microstructure are available in the CC, validation of our results is more complicated in the SC as it is much less documented. Future work needs is required that provides a direct comparison between our MRI parameters and independent histology for a better interpretation of our estimated parameters in healthy tissue but more importantly also in the presence of pathological tissue alteration. Following up on our work on $a\mathcal{SF}$, we are now in the process of setting a validation study of our protocol using post-mortem human spinal cord of healthy and MS tissue in collaboration with XXXXX.

1.5   Conclusion

We have demonstrated that our microstructure estimates agree with reported post-mortem evaluation of the CC fibre density distribution. Further, we showed good inter- and intra-subject reproducibility. The scan time of the protocol is short enough to be easily incorporated into clinical studies. In future work, we are planning to use this approach in subjects with known altered microstructure of the CC.

Bibliography

Alexander, D. C. (2008). A general framework for experiment design in diffusion MRI and its application in measuring direct tissue-microstructure features. *Magnetic Resonance in Medicine*, *60*(2), 439–448.

Alexander, D. C., Hubbard, P. L., Hall, M. G., Moore, E. A., Ptito, M., Parker, G. J. M., & Dyrby, T. B. (2010). Orientationally invariant indices of axon diameter and density from diffusion MRI. *NeuroImage*.

Assaf, Y., Blumenfeld-Katzir, T., Yovel, Y., & Basser, P. J. (2008). AxCaliber: a method for measuring axon diameter distribution from diffusion MRI. *Magnetic Resonance in Medicine*, *59*(6), 1347–1354.

Avram, L., Ã-zarslan, E., Assaf, Y., Bar-Shir, A., Cohen, Y., & Basser, P. J. (2008). Three-dimensional water diffusion in impermeable cylindrical tubes: theory versus experiments. *NMR Biomed.*, *21*(8), 888–898.
URL http://dx.doi.org/10.1002/nbm.1277

Barazany, D., Basser, P. J., & Assaf, Y. (2009). In vivo measurement of axon diameter distribution in the corpus callosum of rat brain. *Brain*.

Cook, P., Bai, Y., Nedjati-Gilani, S., Seunarine, K., Hall, M. G., Parker, G. J. M., & Alexander, D. C. (2006). Camino: open-source diffusion-MRI reconstruction and processing. In *Proceedings 14th Scientific Meeting, International Society for Magnetic Resonance in Medicine*, (p. 2759).

Cook, P. A., Symms, M., Boulby, P. A., & Alexander, D. C. (2007). Optimal acquisition orders of diffusion-weighted MRI measurements. *Journal of Magnetic Resonance Imaging*, *25*(5), 1051–1058.
URL http://dx.doi.org/10.1002/jmri.20905

Golabchi, F. N., Brooks, D. H., Hoge, W. S., Girolami, U. D., & Maier, S. E. (2010). Pixel-based comparison of spinal cord MR diffusion anisotropy with axon packing parameters. *Magnetic Resonance in Medicine*, *63*(6), 1510–1519.

Graf von Keyserlingk, D., & Schramm, U. (1984). Diameter of axons and thickness of myelin sheaths of the pyramidal tract fibres in the adult human medullary pyramid. *Anatomischer Anzeiger*, *157*(2), 97–111.
URL http://ukpmc.ac.uk/abstract/MED/6507887

Panagiotaki, E., Schneider, T., Siow, B., Hall, M. G., Lythgoe, M. F., & Alexander, D. C. (2012). Compartment models of the diffusion MR signal in brain white matter: A taxonomy and comparison. *NeuroImage*, *59*(3),

2241–2254.
URL   `http://www.sciencedirect.com/science/article/pii/`
`S1053811911011566`

Siow, B., Drobnjak, I., Chatterjee, A., Lythgoe, M. F., & Alexander, D. C. (2012). Estimation of pore size in a microstructure phantom using the optimised gradient waveform diffusion weighted NMR sequence. *Journal of Magnetic Resonance*, *214*(0), 51–60.
URL   `http://www.sciencedirect.com/science/article/pii/`
`S1090780711003806`

Stanisz, G. J., Wright, G. A., Henkelman, R. M., & Szafer, A. (1997). An analytical model of restricted diffusion in bovine optic nerve. *Magnetic Resonance in Medicine*, *37*(1), 103–111.
URL `http://onlinelibrary.wiley.com/doi/10.1002/mrm.1910370115/`
`abstract`

Stejskal, E. O., & Tanner, J. E. (1965). Spin diffusion measurements: Spin echoes in the presence of a Time-Dependent field gradient. *Journal of Chemical Physics*, *42*, 288.

Szafer, A., Zhong, J., Anderson, A. W., & Gore, J. C. (1995). Diffusion-weighted imaging in tissues: theoretical models. *NMR in Biomedicine*, *8*(7-8), 289–296.

Wang, Y., Wang, Q., Haldar, J. P., Yeh, F., Xie, M., Sun, P., Tu, T., Trinkaus, K., Klein, R. S., Cross, A. H., & Song, S. (2011). Quantification of increased cellularity during inflammatory demyelination. *Brain*, *134*(12), 3590–3601.
URL `http://brain.oxfordjournals.org/content/134/12/3590`

Zhang, H., Hubbard, P. L., Parker, G. J., & Alexander, D. C. (2011). Axon diameter mapping in the presence of orientation dispersion with diffusion MRI. *NeuroImage*, *56*(3), 1301–1315.
URL   `http://www.sciencedirect.com/science/article/pii/`
`S1053811911001376`